Cell Reports, Volume *42*

Supplemental information

Functional screening of amplification outlier oncogenes in organoid models of early tumorigenesis

Ameen A. Salahudeen, Jose A. Seoane, Kanako Yuki, Amanda T. Mah, Amber R. Smith, Kevin Kolahi, Sean M. De la O, Daniel J. Hart, Jie Ding, Zhicheng Ma, Sammy A. Barkal, Navika D. Shukla, Chuck H. Zhang, Michael A. Cantrell, Arpit Batish, Tatsuya Usui, David E. Root, William C. Hahn, Christina Curtis, and Calvin J. Kuo

Cell Reports, Volume ■ ■

Supplemental information

Functional screening of amplification outlier oncogenes in organoid models of early tumorigenesis

Ameen A. Salahudeen, Jose A. Seoane, Kanako Yuki, Amanda T. Mah, Amber R. Smith, Kevin Kolahi, Sean M. De la O, Daniel J. Hart, Jie Ding, Zhicheng Ma, Sammy A. Barkal, Navika D. Shukla, Chuck H. Zhang, Michael A. Cantrell, Arpit Batish, Tatsuya Usui, David Root, William Hahn, Christina Curtis, and Calvin J. Kuo

Figure S1

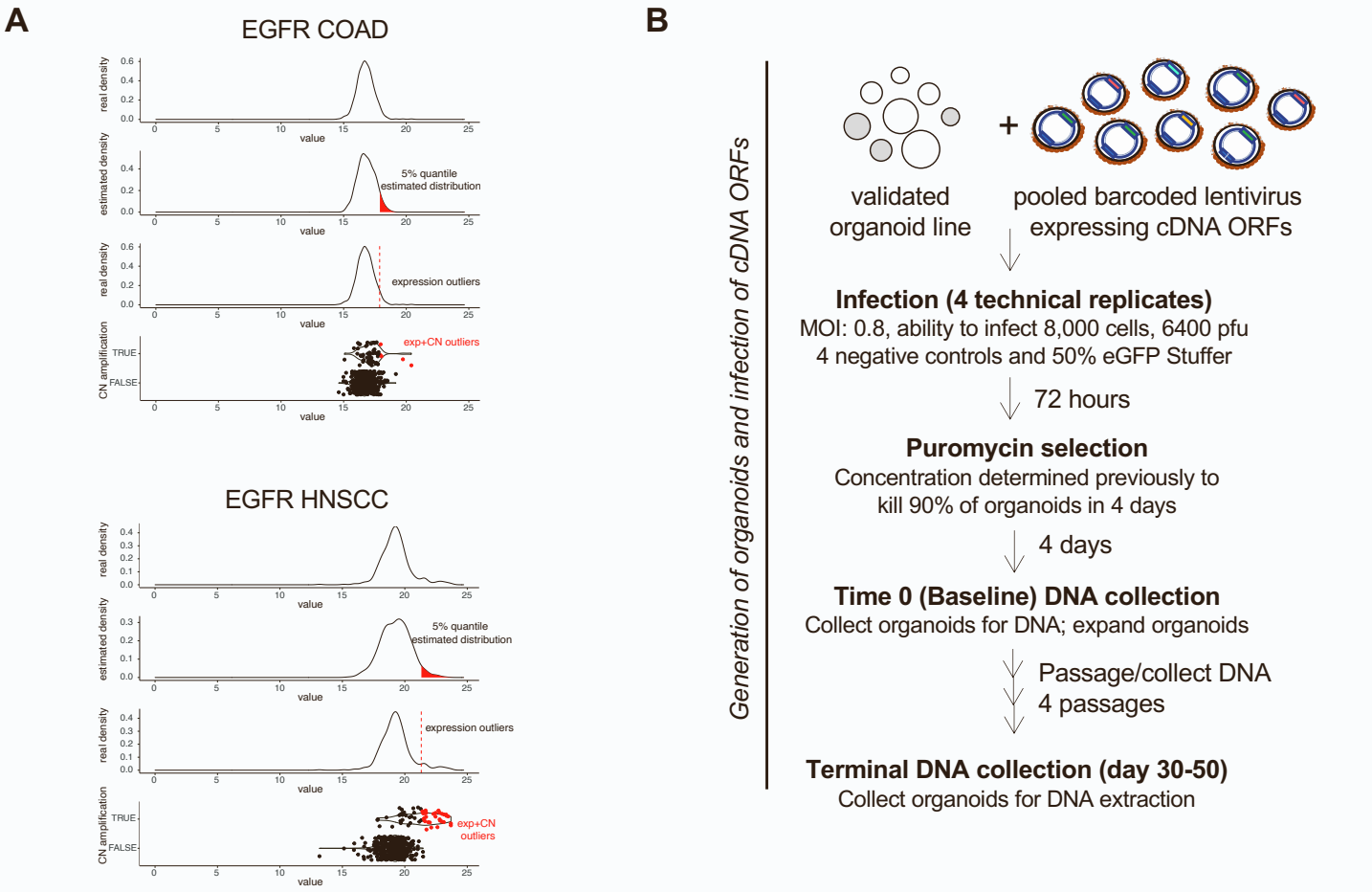

Figure S1. Identification and Validation of candidate SCNA drivers (related to Fig. 1).

A) Schematic of integrative analysis to nominate outlier gene candidates for EGFR in colon adenocarcinoma (COAD) (top) and head and neck squamous carcinoma (HNSCC) (bottom). Top panel shows the expression counts density for EGFR to obtain the mean and standard deviation from these distributions. In the second panel, using the mean and standard deviation, theoretical normal distributions were generated and the 5% quantile of higher expression (red colored distribution) was used to define a threshold that was later applied to the original distribution (red line, third panel). Samples with expression higher than these thresholds were classified as expression outliers. In the last panel the boxplots shows the distribution of expression across copy number amplified and not amplified samples. The final outlier list is the intersection between the amplified samples and the expression outliers and the amplification in the COAD samples lack an effect in the expression, thus most of the amplified samples are not classified as outliers. In contrast, in HNSC (bottom panels) there is a significant number of CN amplified samples with a subsequent change in expression resulting in greater number of amplified samples being classified as outliers.

B) Schematic of pooled ORF screening experiments in this study.

Figure S2

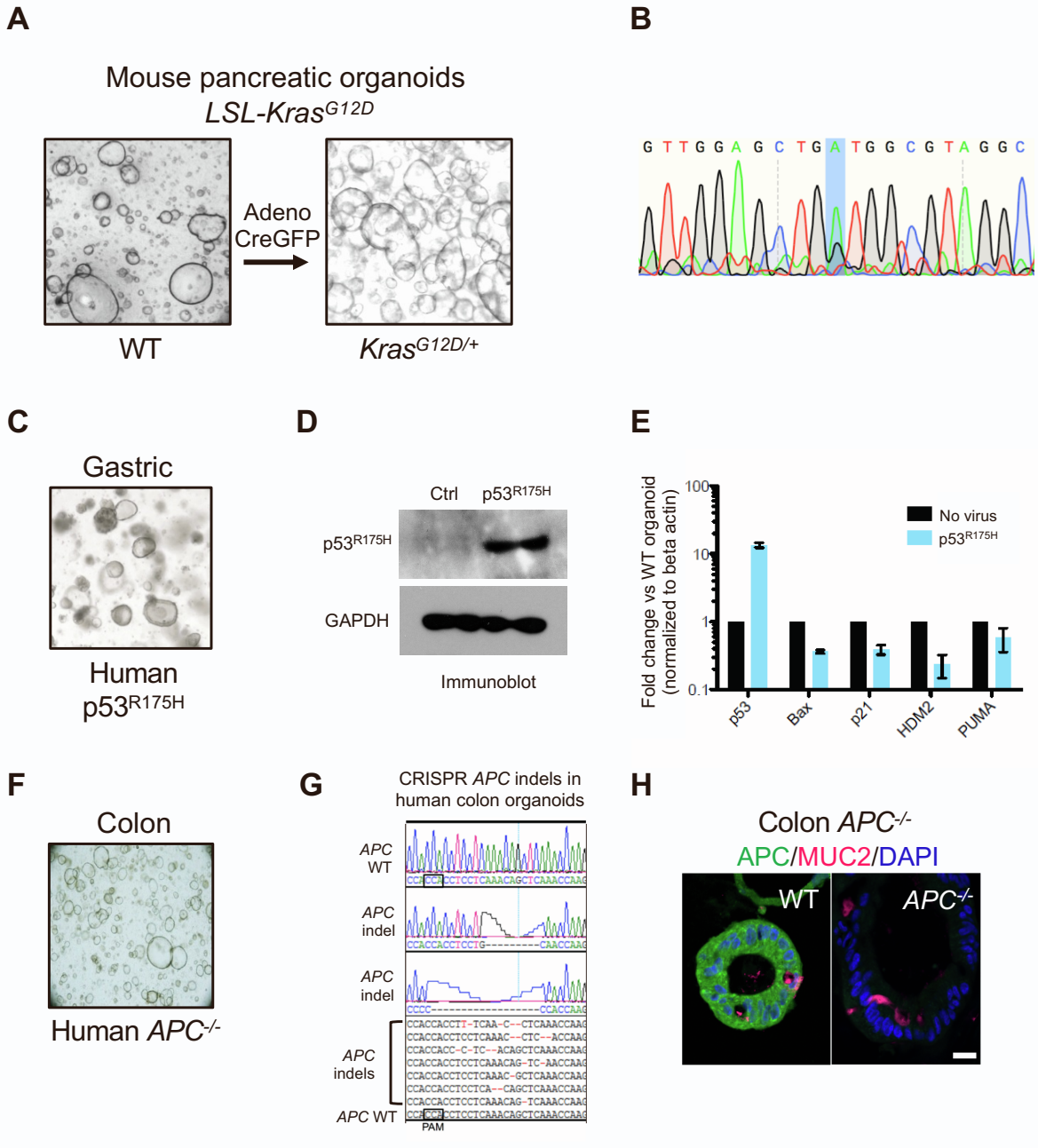

Figure S2. Generation and validation of tissue contextual models of pancreatic, gastric, and colon carcinomas (related to Fig. 1)

A) Schematic of *Kras*^{G12D} pancreatic organoid derivation.
B) Sanger sequencing of *Kras* cDNA.
C) Brightfield microscopy of human gastric *p53*^{R175H} organoids.
D) Immunoblotting of p53^{R175H} in transduced versus control gastric organoids.
E) qRT-PCR of *p53* target genes in transduced versus control gastric organoids. Each group had n = 3 technical replicates. Data represent mean ± SEM.
F) Brightfield microscopy of human colon *APC*$^{-/-}$ organoids.
G) Sanger tracing of TA cloned genomic PCR amplicons of the CRISPR KO *APC* locus demonstrating indel mutagenesis.
H) Immunofluorescence of wild type versus *APC* CRISPR KO human colon organoids.

Figure S3

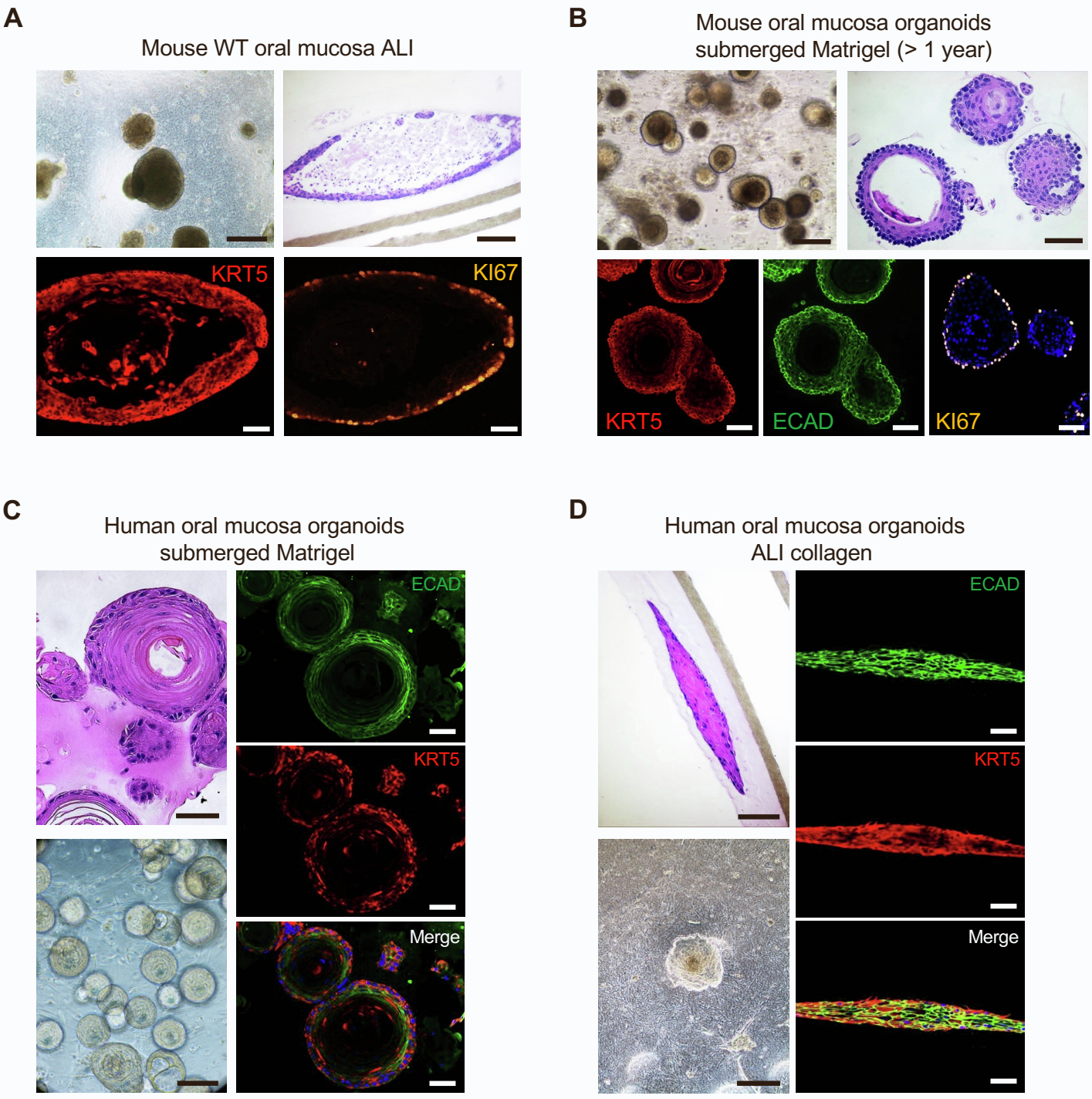

Figure S3. Evaluation of murine and human oral mucosal organoids in submerged Matrigel and ALI (related to Fig. 2)

A) WT mouse oral mucosa organoids cultured in ALI for 34 days. Scale bar: brightfield; 500 µm (left top panel), H&E staining; 100 µm (right top panel), IF staining; 50 µm (bottom panels).
B) Submerged Matrigel cultures of wild type murine oral mucosa organoids at day 9, scale bars: brightfield; 200 µm, H&E staining; 50 µm, IF staining; 50 µm.
C) Submerged Matrigel cultures of normal human oral mucosa at day 13, scale bars: H&E staining; 50 µm, brightfield; 100 µm, IF staining; 50 µm.
D) Air-liquid interface cultures of normal human oral mucosa at day 18, scale bars: H&E staining; 100 µm, brightfield; 500 µm, IF staining; 50 µm.

Figure S4

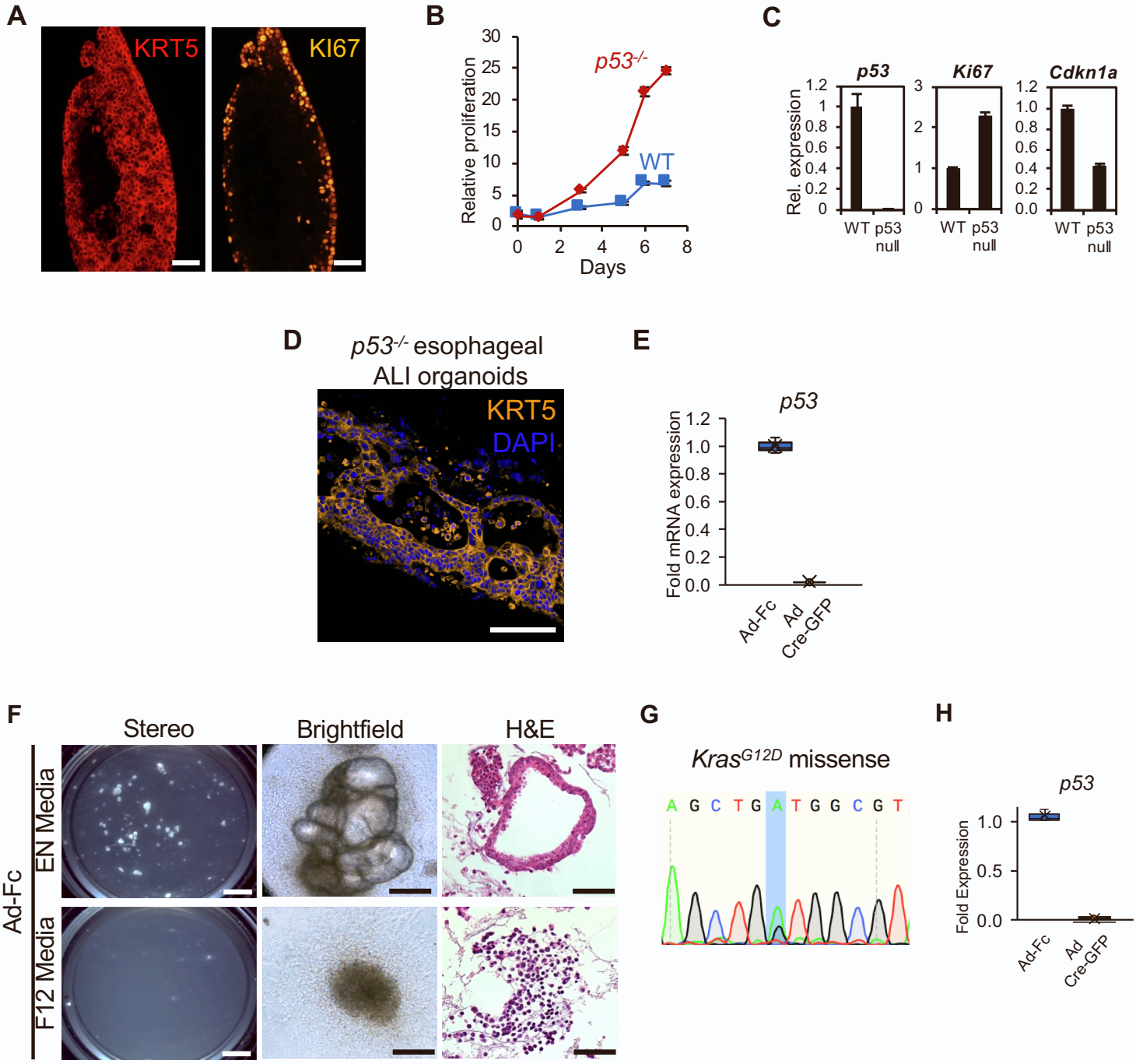

Figure S4. Evaluation of murine oral, esophageal, and lung organoids (related to Fig. 2)

A) KRT5 IF staining (left panel) and KI67 IF staining (right panel) of *p53*$^{-/-}$ mouse oral mucosa organoids cultured in ALI for 34 days, Scale bar: 50 μm.
B) Proliferation of oral mucosa p53-/- and WT organoids in ALI culture assessed by resazurin reduction. Each group had n = 3 technical replicates. Data represent mean ± SEM.
C) qRT-PCR of p53, Ki67 and Cdkn1a, in p53$^{-/-}$ versus WT mouse oral mucosa organoids in ALI. Each group had n = 3 technical replicates. Data represent mean ± SEM. *P* < .001 between groups, two tailed student's t-test.
D) KRT5 immunofluorescence of p53$^{-/-}$ mouse esophageal organoids from serial FFPE section from right panel of Fig. 2D.
E) qRT-PCR of p53 mRNA in Ad-Fc- or Ad-Cre-GFP-infected p53flox/flox esophageal organoids. Each group had n = 3 technical replicates. *P* < .001 between groups, two tailed student's t-test.
F) Microscopy of lung organoids without activation of latent Kras$^{LSL-G12D}$; p53$^{flox/flox}$ alleles in complete (EN) versus minimal (F12) media. Left, stereomicroscopy of organoids at d28, Middle, phase contrast microscopy of organoids at d28, Right, H&E staining of organoid cultures at d28. Scale bars = 3 mm, 250 μm, and 250 μm respectively.
G) Sanger sequencing of Kras cDNA upon activation of latent LSL KrasG12D.
H) qRT-PCR of p53 in Ad-Fc or Ad-Cre-GFP infected KrasG12D; p53-/- lung organoids. Each group had n = 3 technical replicates. P < .001 between groups, two tailed student's t-test.

Figure S5

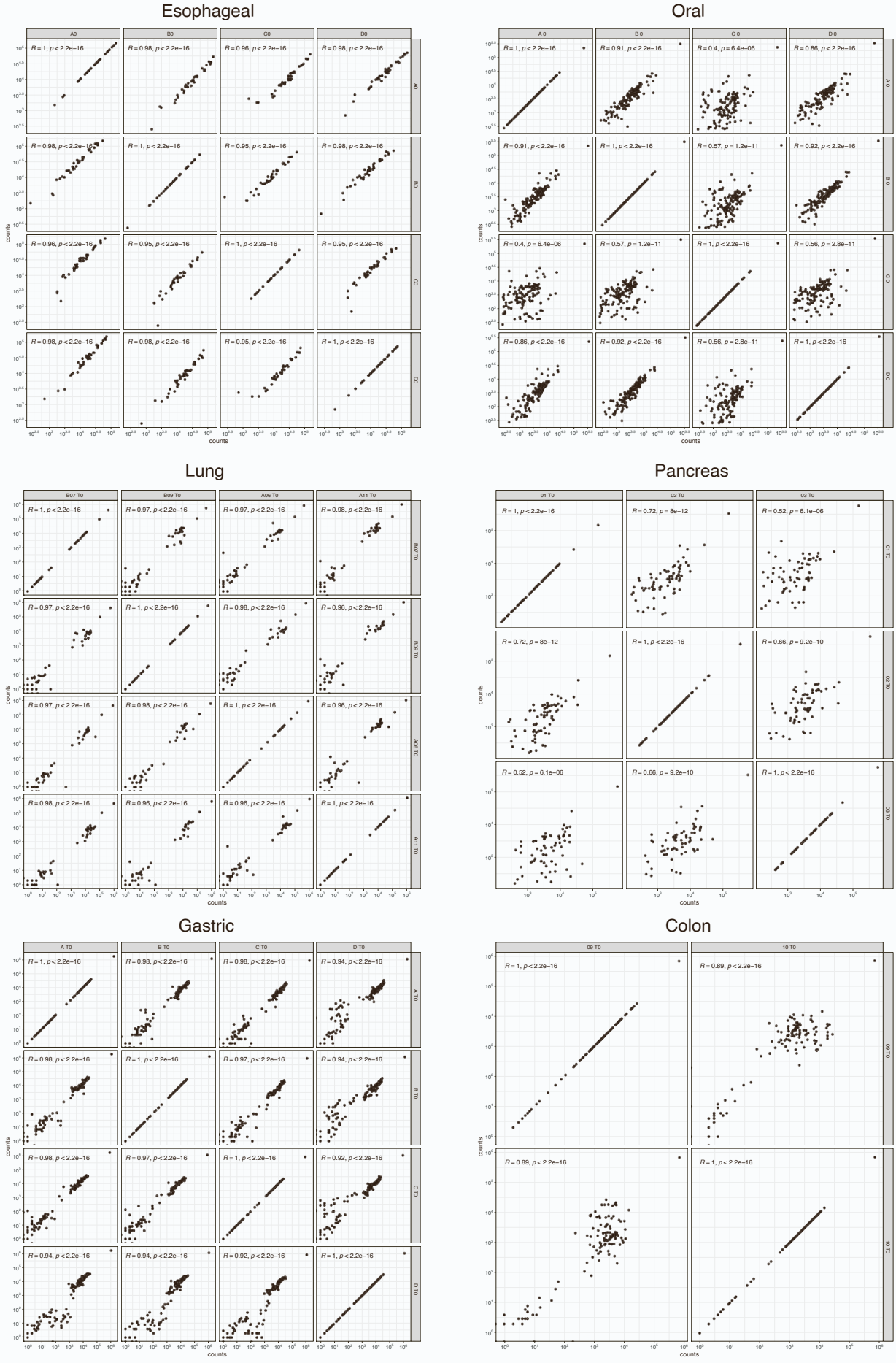

Figure S5. Scatterplots correlating barcode counts of timepoint zero biological replicates. Correlation is calculated with Pearson correlation and correlation p-value is calculated using cor.test (related to Fig. 3).

Figure S6

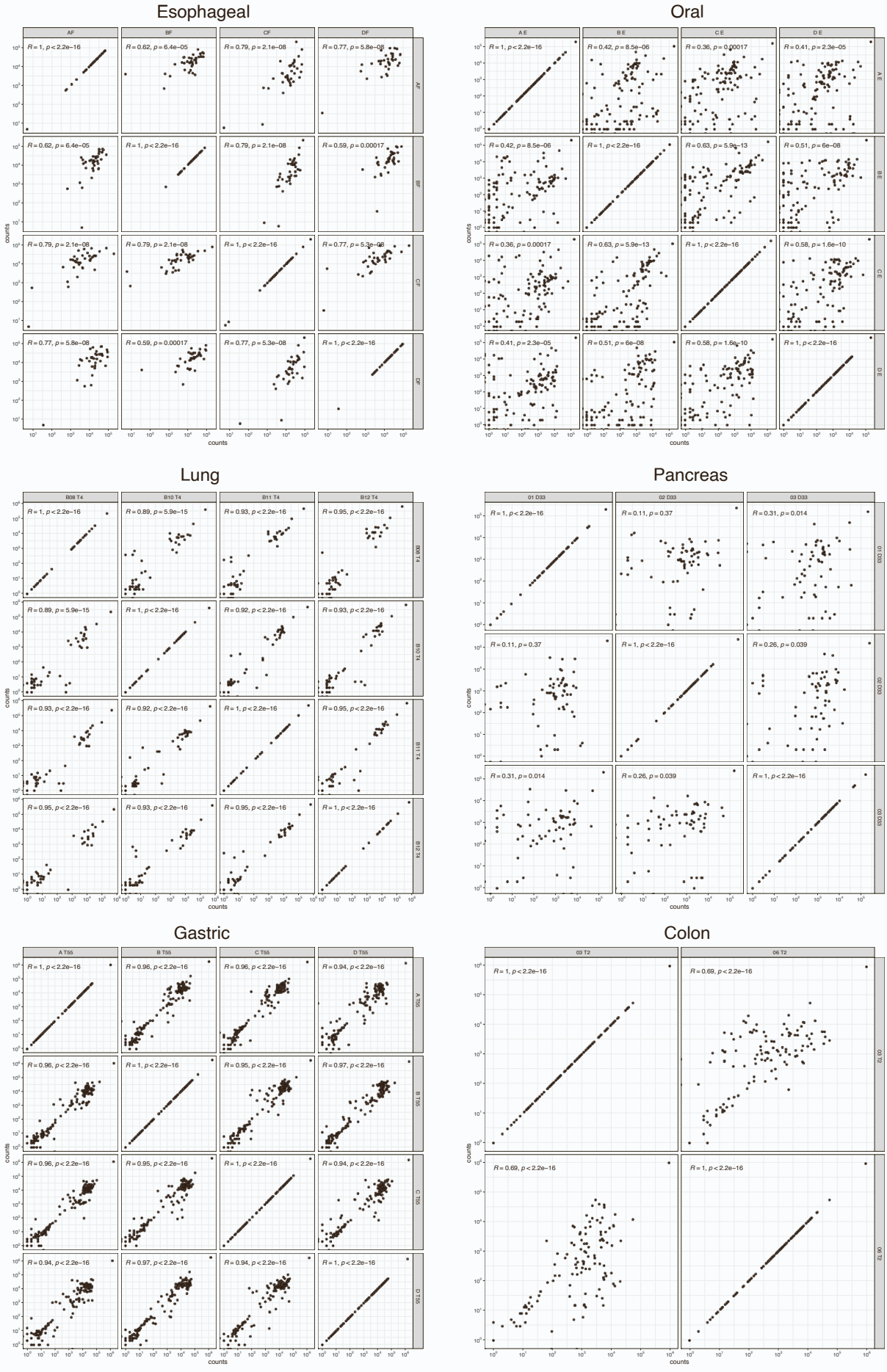

Figure S6. Scatterplots correlating barcode counts of terminal timepoint biological replicates. Correlation is calculated with Pearson correlation and correlation p-value is calculated using cor.test (related to Fig. 3).

Figure S7

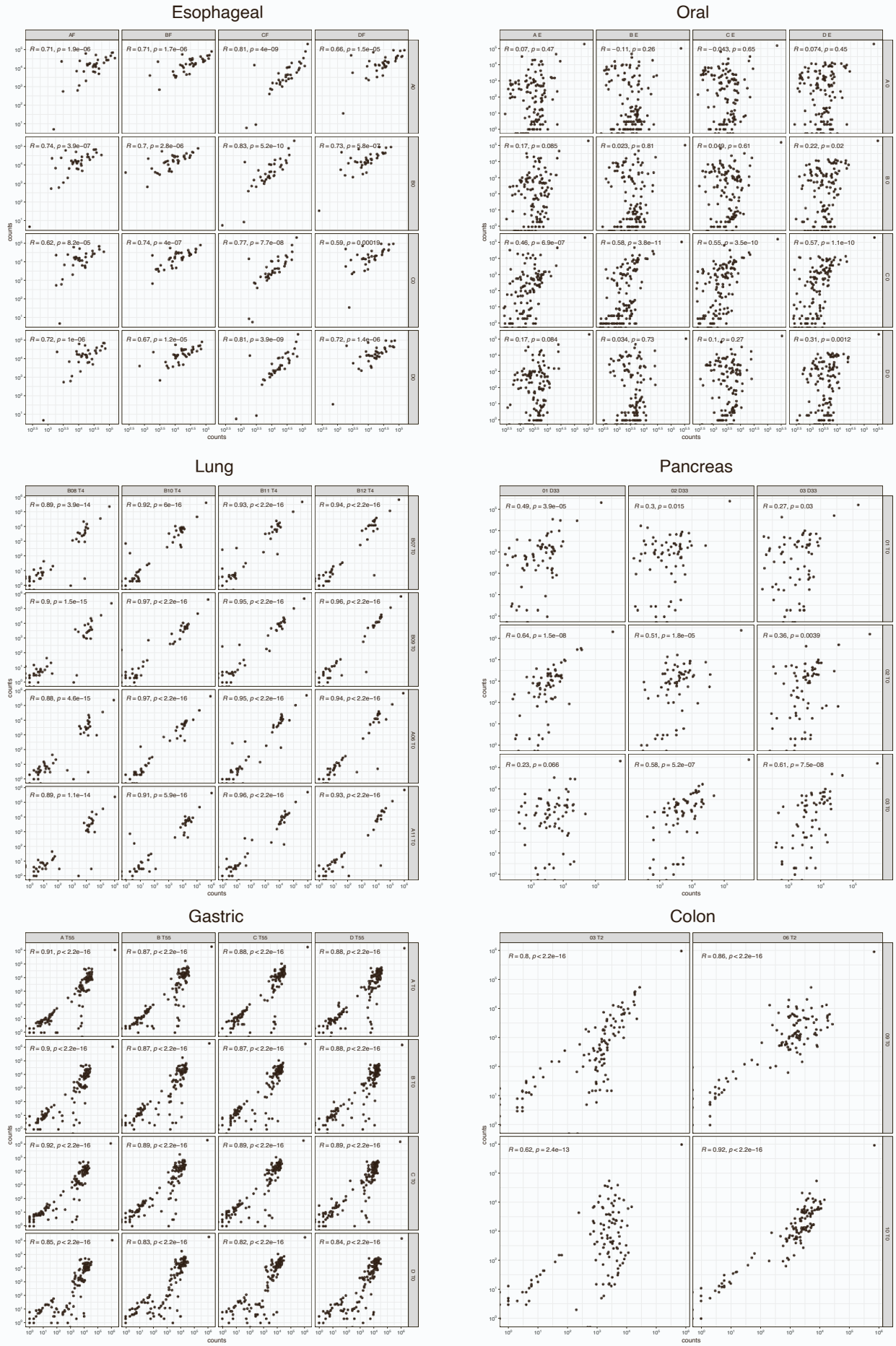

Figure S7. Scatterplots correlating barcode counts of terminal timepoint versus time point zero across biological replicates. Correlation is calculated with Pearson correlation and correlation p-value is calculated using cor.test (related to Fig. 3).

Figure S8

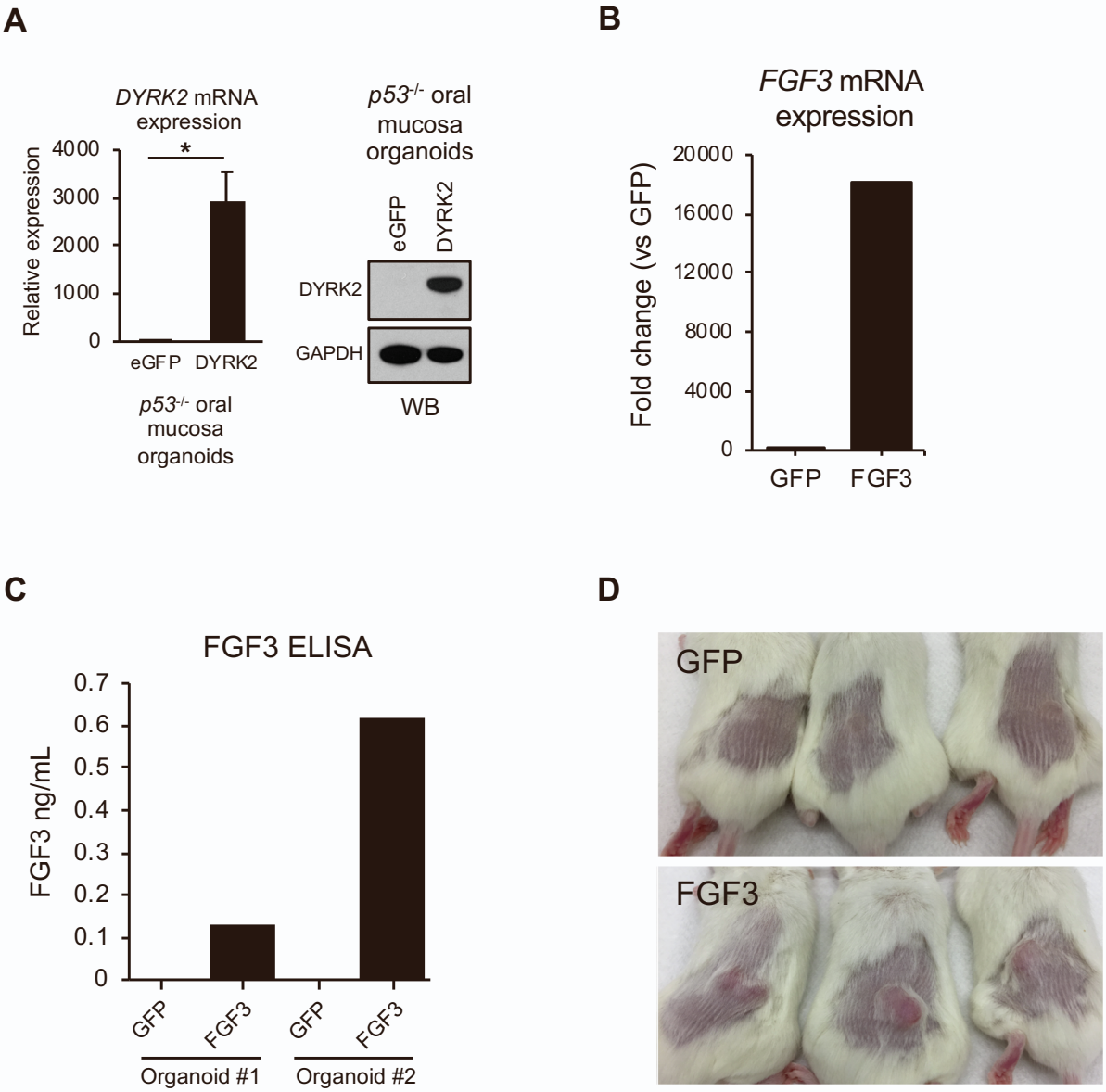

Figure S8. Characterization of DYRK2 and FGF3 overexpression in p53$^{-/-}$ oral mucosa and esophageal organoids respectively.

A) DYRK2 qRT-PCR (left) and immunoblot (right) in GFP vs DYRK2 expressing *p53*$^{-/-}$ oral mucosa organoids. Data represent mean ± SEM. $P < .05$ between groups, two tailed student's t-test.

B) qRT-PCR of FGF3 mRNA in GFP and FGF3 expressing *p53*$^{-/-}$ esophageal organoids. Each group had n = 3 technical replicates. Data represent mean ± SEM.

C) Bar plots of FGF3 ELISA measurements in organoid conditioned media.

D) Photographs of subcutaneous tumor formation of GFP expressing and FGF3 expressing *p53*$^{-/-}$ esophageal organoids.

Figure S9

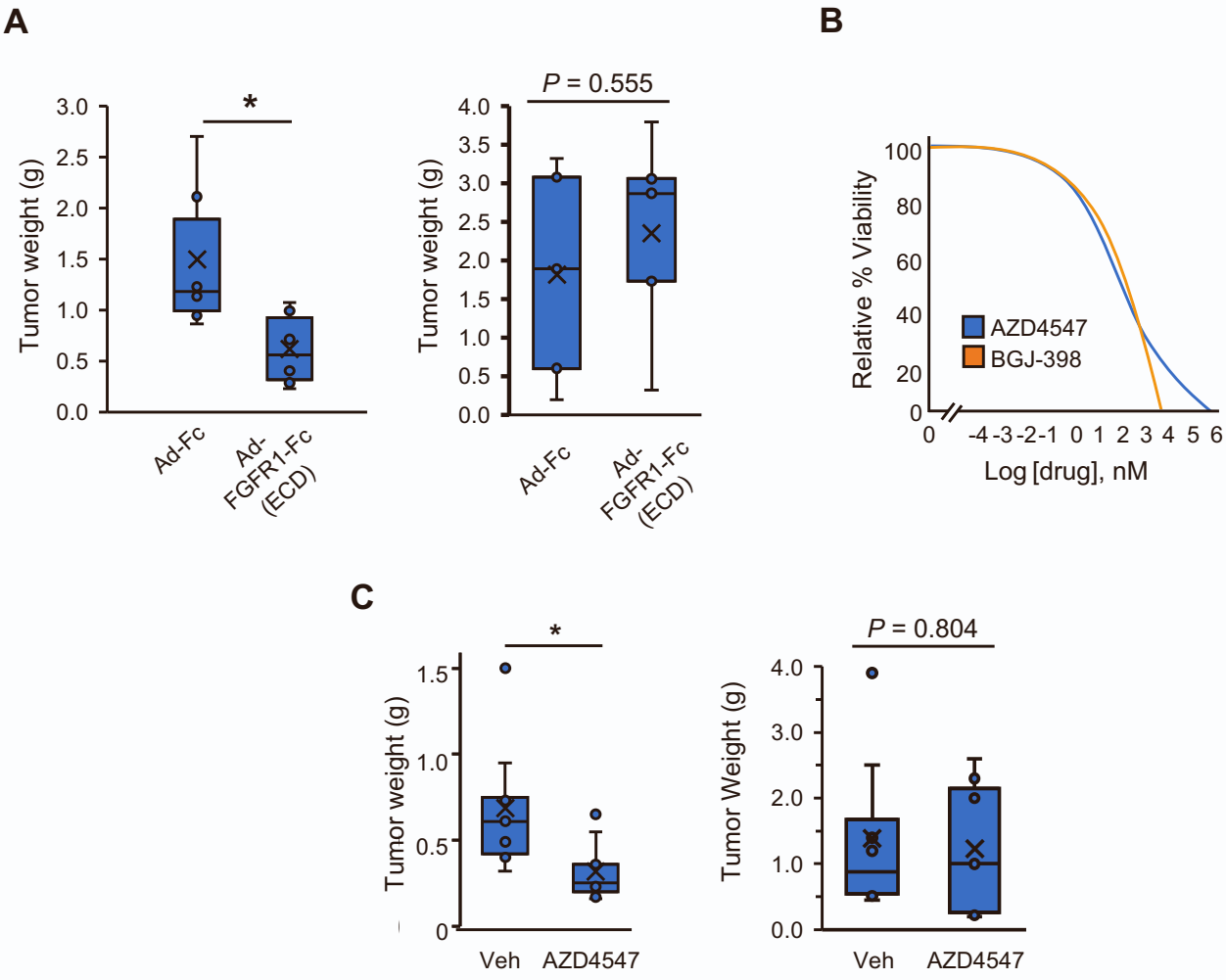

Figure S9. Evaluation of mechanisms of FGF3 mediated tumorigenesis in *p53*$^{-/-}$ esophageal organoids (related to Fig. 5)

A) Terminal tumor weights of Fig. 5I. * = $P < 0.05$ two tailed student's t-test.
B) Fitted dose response curves of BGJ398 (EC_{50} = 567 nM) and AZD4547 (EC_{50} = 348 nM) FGFR inhibitors on *p53*$^{-/-}$; FGF3 esophageal organoids in basal F12 media. Each group had n = 3 technical replicates. *p53*$^{-/-}$; GFP organoids are unable to proliferate in basal F12 media.
C) Terminal tumor weights of Fig. 5J. * = $P < 0.05$ two tailed student's t-test.